**Michigan
Technological
University**
1885

Dissertations, Master's Theses and Master's Reports

2021

PHASE-FIELD FRACTURE MODELING FOR INTERLOCKING MICRO-ARCHITECTURED MATERIALS

Shubham Sinha
Michigan Technological University, shsinha@mtu.edu

Follow this and additional works at: https://digitalcommons.mtu.edu/etdr

Part of the Applied Mechanics Commons, and the Computer-Aided Engineering and Design Commons

PHASE-FIELD FRACTURE MODELING FOR INTERLOCKING MICRO-ARCHITECTURED MATERIALS

By

Shubham Sinha

A REPORT

Submitted in partial fulfillment of the requirements for the

degree of

MASTER OF SCIENCE

In Mechanical Engineering

MICHIGAN TECHNOLOGICAL UNIVERSITY

2021

This report has been approved in partial fulfillment of the requirements for the Degree of MASTER OF SCIENCE in Mechanical Engineering.

Department of Mechanical Engineering - Engineering Mechanics

Report Advisor: *Susanta Ghosh*

Committee Member: *Parisa Pour Shahid Saeed Abadi*

Committee Member: *Sajjad Bigham*

Department Chair: *William W. Predebon*

Contents

Acknowledgement

Abstract

It is fascinating to see how natural materials like teeth enamel, bone and nacre possess a very high stiffness and strength in spite of the fact that they are composed of minerals mostly. Studies have shown the reason for this aberration as the presence of weaker interfaces with intricate interlocking architectures at microscopic levels in these materials. Inspired by the architecture of these materials, micro-architectured sutures with jig-saw like geometry is being studied in this research study. The main focus of this study is to examine the effects of friction co-efficient and interlocking angles of the jig-saw tabs on pullout strength, fracture toughness and energy absorption. We are using Phase-Field Fracture model to study these effects in ABS (acrylonitrile-butadiene-styrene) material. We will also simulate the fracture of the interlocking tabs when the interlocking angle goes beyond a certain limit.

Chapter 1

Introduction

Fracture is one of those criterion which if not analysed properly can result in destructive outcomes. Fracture in brittle material is of main concern as it can occur without any warning and it is cumbersome to study the initiation and propagation of cracks in brittle materials.

It was Griffith [1] who first gave the theory of crack evolution in brittle materials. Following which, Inglis [2] introduced a very important parameter, Stress Intensity Factor, that gave us an idea about stress distribution near and around the crack tip. Griffith and Inglis considered energy release rate as the driving force behind opening of cracks. These theories could not describe crack initiation, branching and curvilinear crack paths; however, they contributed towards the development of a number of techniques to solve fracture problems computationally.

One of such computational technique to solve fracture problem is the Phase-Field Fracture model [3,4]. It is more robust in comparison to other methods like node-splitting [5] and cohesive surfaces [6] where a discrete crack is needed and crack can propagate only between the elements. This makes the crack propagation strongly dependent on mesh and the method is computationally more expensive.On the contrary, phase-field approach considers crack as a smeared/diffused damage. Here the damage is estimated by using a scalar function whose value lies between zero and one, and this scalar function is estimated by an energy minimization variational process [7-11]. This method is capable to simulate crack branching and curvilinear paths which were the limitations of the discrete crack methods.

In this study we are studying the design of micro-architectured sutures with jig-saw puzzle like geometry, which is inspired by the architecture of natural materials like teeth enamel, bone and nacre [12]. These materials are majorly composed of minerals, however, they exhibit a very unique combination of strength, toughness and durability [13-15]. The reason for this unique and anomalous behavior is the intricate architecture of building blocks that are connected via weak interfaces [16]. These interfaces play a vital role as they help channelize the crack along the interface, thus increasing the deformation along with helping in the dissipation of energy through large volumes of bulk materials [17]. Implementing sutures with jig-saw puzzle like geometry gives similar response as it is seen in these materials [18]. We are implementing the Phase-Field model to study the effect of friction coefficient and interlocking angle of the jig-saw tabs on the pullout strength, ductility, deformability and fracture. The novelty of this computational approach is the simulation of fracture of tabs which have only been done experimentally before. It will be seen that for a certain interlocking angle of the jig-saw tabs, the tabs break before they are completely pulled apart.

Chapter 2

Theory of Phase-Field Fracture

2.1 Phase-Field Approach & Crack surface

Let us consider an infinitely long 1D bar as shown in Fig. 2.1. It contains a sharp crack as shown at x=0. If we denote this crack with $d(x)$ then

$$d(x) = 1 \; at \; x = 0, \; \; d(x) = 0 \; at \; x = \pm\infty \tag{2.1}$$

Thus, the function d(x) is dirac-delta function here.
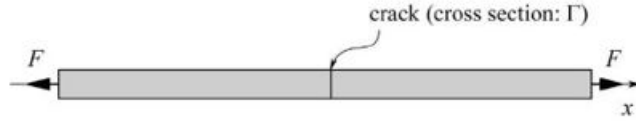

Figure 2.1: 1D bar with sharp crack at x = 0 (Source: Molnar, [19])

Now it is known that the energy released (ψ) due to this crack can be calculated by multiplying the critical fracture energy release rate G_c with the crack surface area (A), which is nothing but the cross-sectional area of bar at x=0 (2.2).

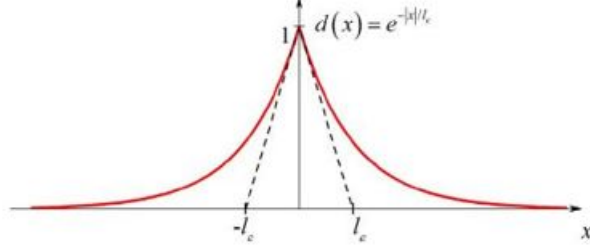$$\psi = \int_\Gamma G_c d\Gamma = G_c A \tag{2.2}$$

Figure 2.2: Diffused Crack (Source: Molnar, [19])

This is simple to find in case of 1D geometry, however, it becomes burdensome to find the energy dissipated due to the cracks in higher dimensions as we need the idea of crack path and its propagation.This is where Phase-Field approach as shown by Miehe [4] comes into the picture by considering crack as a diffused/smeared damage rather than a sharp discontinuity. Phase-field considers the function $d(x)$ as an exponential function (2.3) whose value lies between 0 and 1. The diffused crack has been shown in Fig. 2.2. Through this method we can calculate the crack surface area by integration over a given domain and can easily obtain the energy dissipation due to fracture in higher dimensional problems.

$$d(x) = e^{-\frac{|x|}{l_c}} \tag{2.3}$$

Here, l_c is the length scale parameter and $d(x)$ is the diffused/smeared damage. If $l_c = 0$, the crack becomes sharp.

The function $d(x)$ in (2.3) is the solution to the homogeneous differential equation,

$$d(x) - l_c^2 d''(x) = 0 \quad in \quad \Omega \tag{2.4}$$

subjected to the Dirichlet boundary conditions in (2.1).

The quadratic functional can be obtained from the Galerkin-Weak form of (2.4) and is given by,

$$I(d) = \frac{1}{2} \int_{\Omega} (d^2 + l_c^2 \, d'^2) dV \tag{2.5}$$

Thus, it can be said that the differential equation (2.4) is the Euler-Lagrange

8

equation of the variational form,

$$d = \arg\{\inf_{d \in W} I(d)\} \tag{2.6}$$

where $W = \{d | d(0) = 1, \, d(\pm\infty) = 0\}$.

Now if $dV = \Gamma dx$, it can be shown from (2.5) that

$$I(d = e^{-\frac{|x|}{l_c}}) = l_c \Gamma \tag{2.7}$$

From (2.7) we can derive the relation between Γ and $I(d)$ as,

$$\Gamma(d) = \frac{1}{l_c} I(d) \tag{2.8}$$

$$or, \Gamma(d) = \frac{1}{2l_c} \int_\Omega (d^2 + l_c^2 \, d'^2) dV = \int_\Omega \gamma(d, d') dV \tag{2.9}$$

$\gamma(d, d')$ is the crack surface density function per unit volume in 1D. Equivalently, in higher dimension the crack surface density function can be written as,

$$\gamma(d, \nabla d) = \frac{1}{2l_c} d^2 + \frac{1}{2l_c} \nabla d^2 \tag{2.10}$$

2.2 Energy Degradation

The potential energy of a solid body due to fracture can be written as,

$$\Pi^{int} = E(\mathbf{u}, d) + W(d) \tag{2.11}$$

where $E(u, d)$ is the strain energy and $W(d)$ is the fracture energy in the solid.

The above calculation of crack surface was limited to one-dimension but we can easily extend this concept into higher dimensions by expressing the solid configuration as $\Omega \subset \mathrm{R}^\delta$, where $\delta \in (1,2,3)$, and $\delta\Omega \subset \mathrm{R}^{\delta-1}$ represents the surface of the solid. In this study we are studying time dependent crack phase-field and displacement fields where $T \subset \mathrm{R}$ [4]. The time-dependent phase-field can be represented as,

$$d : \begin{cases} \Omega \times T \to [0, 1] \\ (\mathbf{x}, t) \to d(\mathbf{x}, t). \end{cases} \tag{2.12}$$

and the diplacement-field as,

$$u : \begin{cases} \Omega \times T \to R^\delta \\ (\mathbf{x}, t) \to u(\mathbf{x}, t). \end{cases} \tag{2.13}$$

Now from Eq. (2.11), E(u,d) is the internal potential energy and can be expressed as,

$$E(\mathbf{u}, d) = \int_\Omega \psi(\epsilon(\mathbf{u}), d) dV \tag{2.14}$$

where $\psi(\epsilon, d)$ is the internal potential energy density and can be written as,

$$\psi(\epsilon, d) = g(d).\psi_0(\epsilon) \tag{2.15}$$

In Eq.(2.15), $\psi_0(\epsilon)$ is the internal strain energy density of the undamaged material and g(d) is called a degradation function [19], such that

$$g(d) = (1 - d)^2 + k \tag{2.16}$$

k is a very small constant added for the numerical stability of the solution.

Eq. (2.15) is only valid for isotropic models, i.e, the full stress tensor is degraded if this model is considered. This results in the energy release due to fracture in both tension and compression cases. Isotropic model is limited for cases that involves only tensile stresses. Thus, to overcome this model, anisotropic energy degradation was introduced [4]. In this case only the tensile part of stress tensor is degraded and the internal potential energy density is given as,

$$\psi(\epsilon, d) = g(d).\psi_0^+ + \psi_0^- \tag{2.17}$$

ψ_0^+ is the elastic strain energy density due to tension and ψ_0^- is the elastic strain energy due to compression. Now considering the unbroken/undamaged material as elastic, stress tensor can be written as,

$$\sigma_0 = \mathbf{C_0}\epsilon \tag{2.18}$$

and the strain energy density as,

$$\psi_0 = \frac{1}{2}\epsilon^\mathbf{T}\mathbf{C_0}\epsilon \tag{2.19}$$

Here, ϵ is the vector of strain components and is given by,

$$\epsilon = \frac{1}{2}((\nabla \mathbf{u})^T + (\nabla \mathbf{u})) \tag{2.20}$$

Now, by differentiating Eq. (2.15) with respect to the strain tensor we get,

$$\sigma = g(d).\sigma_0 = [(1 - d)^2 + k].\mathbf{C_0}\epsilon \tag{2.21}$$

Similarly we can write,

$$\mathbf{C} = [(1 - d)^2 + k].\mathbf{C_0} = g(d).\mathbf{C_0} \tag{2.22}$$

It is evident from the above equations that along with strain energy, there is also a degradation of stress and stiffness matrix.

The other term in the internal potential energy expression in Eq. (2.11) is $W(d)$. This is the energy released due to fracture and can be written as,

$$W(d) = \int_\Omega G_c \, \gamma(d, \nabla d) dV \tag{2.23}$$

$W(d)$ denotes the summation of energy released due to all the crack surfaces that generated due to fracture.

Finally the external potential energy can be written as,

$$\Pi^{ext} = \int_{\mathbf{\Omega}} \overline{\gamma}.\mathbf{u}dV \; + \; \int_{\delta\mathbf{\Omega}} \overline{t}.\mathbf{u}dA \tag{2.24}$$

where, $\overline{\gamma}$ and $\overline{t}$ are the body and the surface forces acting on the body respectively.

2.3 Staggered approach for phase-field solution

Fig. 2.3 gives a schematic representation of how the phase-field problem is solved using staggered method. Here, we solve the problem by dividing it into two different energy minimization process. The first functional that will be minimized to find phase-field is given as,

$$\Pi^d = \int_\Omega [G_c \, \gamma(d, \nabla d) + (1 - d)^2 H] \, dV \tag{2.25}$$
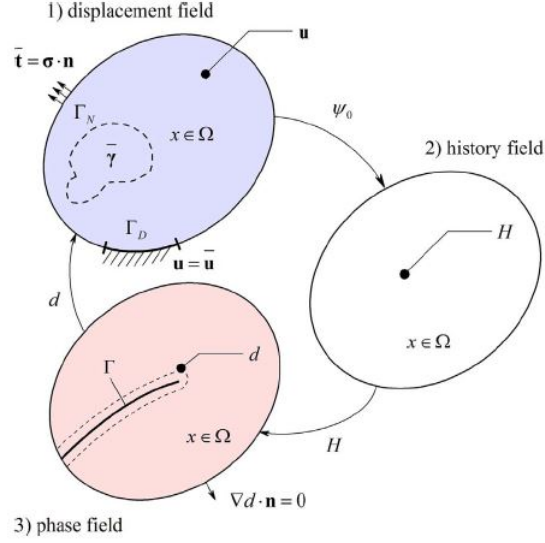
Figure 2.3: Schematic representation of staggered phase-field problem (Source: Molnar, [19])

where H is called history function and can be represented as follow:

$$H = \begin{cases} \psi_0(\epsilon) & \text{if } \psi_0(\epsilon) > H_n \\ H_n & \text{otherwise} \end{cases} \tag{2.26}$$

where H_n is the energy calculated at the previous step n. This history function not only couples the phase-field and displacement, but it also takes care of irreversibility of damage by preventing any reduction in damage value, i.e, $d' \geq 0$ is always satisfied.

Now, the functional to solve for displacement is given as,

$$\Pi^u = \int_\Omega [\psi(\mathbf{u}, d) + \overline{\gamma}.\mathbf{u}] \, dV - \int_{\delta\Omega} \overline{\mathbf{t}}.\mathbf{u} \, dA \tag{2.27}$$

Finally by finding the first variation of Eqs. (2.25) and (2.27) we can write the strong form for phase-field and displacement field as shown in Eqs. (2.28) and (2.29) respectively.

Phase-field strong form:

12

$$\delta\Pi^d = 0 \;\; \forall \;\; \delta d \rightarrow \;\; \frac{G_c}{l_c}(d - l_c^2 \Delta d) = 2(1-d)H \text{ in } \Omega, \text{ and}$$

$$\nabla d.\mathbf{n} = 0 \text{ in } \Gamma. \tag{2.28}$$

Displacement field strong form:

$$\delta\Pi^u = 0 \;\; \forall \;\; \delta u \rightarrow \;\; \nabla\sigma - \overline{\gamma} = 0 \text{ in } \Omega$$

$$\sigma.\mathbf{n} = 0 \text{ on } \Gamma_N$$

$$u = \overline{u} \text{ on } \Gamma_D \tag{2.29}$$

2.4 Finite Element Implementation

The phase-field fracture problem is solved through Abaqus User Defined Elements (UEL) where the two minimization problems given in Eq. (2.25) and Eq. (2.27) are solved iteratively. First Eq. (2.25) is solved to find the phase-field at time t_{n+1} based on the quantities obtained at time t_n, and can be written as,

$$d_{n+1} = \arg\{\inf_d \int_\Omega [G_c \; \gamma(d, \nabla d) + (1-d)^2 H] \; dV\} \tag{2.30}$$

Using Newton-Raphson method, the linear equation obtained through the above minimiation can be solved as,

$$\mathbf{K_n^d d_{n+1}} = -\mathbf{r_n^d} \tag{2.31}$$

where, $\mathbf{d_{n+1}}$ is the vector containing phase-field values at all integration points at time t_{n+1}, $\mathbf{K_n^d}$ is the stifness matrix at time t_n and $\mathbf{r_n^d}$ is the residual vector at time t_n.

Similarly we can solve for the displacement field at time t_{n+1} from the other quantities obtained at time t_n through the following minimization process,

$$u_{n+1} = \arg\{\inf_u \int_\Omega [\psi(\mathbf{u}, d) \; + \overline{\gamma}.\mathbf{u}] \; dV - \int_{\delta\Omega} \overline{t}.\mathbf{u} \; dA\} \tag{2.32}$$

Similar to Eq. (2.31), this problem can be solved as,

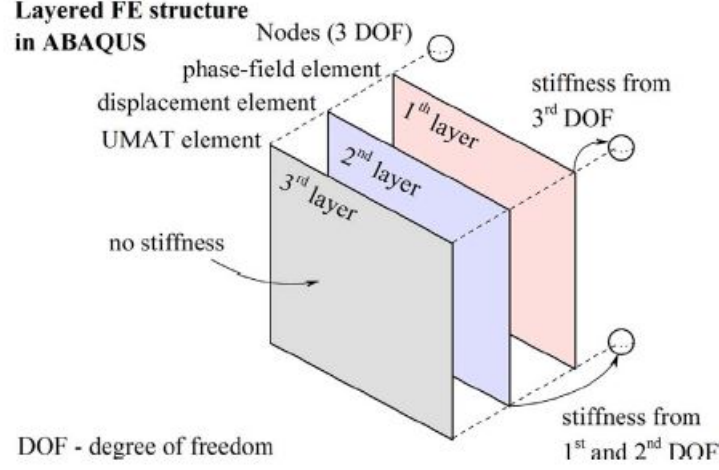$$\mathbf{K_n^u u_{n+1}} = -\mathbf{r_n^u} \tag{2.33}$$

Figure 2.4: Schematic representation of the three layered UEL (Source: Molnar, [19])

Molnar [19] used two 4 noded isoparametric 2D element types in Abaqus to obtain the solution. Fig 2.4 clearly explains the implementation. The first layer is utilized to store the phase-field values and thus only has one degree of freedom (DOF). On the other hand, the second layer is used to store the displacement values and can have two or three DOF based on the dimensionality of the material. It is not possible to visualize the user defined elements (UEL) in Abaqus. Thus, apart from these two layers there is an additional UMAT layer added to the UEL. Table 2.1 & 2.2 show the various State Dependent Solutions obtained from the Abaqus simulation.

The staggered scheme connects the two element layers through the common block and solves the system of linear equations in Eq. (2.31) and (2.33) iteratively using Newton-Raphson method as shown below,

$$\begin{bmatrix} \mathbf{K_n^d} & 0 \\ 0 & \mathbf{K_n^u} \end{bmatrix} \begin{bmatrix} \mathbf{d_{n+1}} \\ \mathbf{u_{n+1}} \end{bmatrix} = - \begin{bmatrix} \mathbf{r_n^d} \\ \mathbf{r_n^u} \end{bmatrix} \tag{2.34}$$

Fig. 2.5 can explain this iterative solution clearly. In this approach, the history function $\psi_{0,n}$ obtained by the displacement element at n^{th} time step is utilized by the phase-field element to calculate the damage value d_{n+1} at

14

Solution Dependent Variables (SDV) in Displacement Element	
Variable	2D (x,y)
Displacement - u_x, u_y	SDV1 - SDV2
Axial Strains - ϵ_x, ϵ_y	SDV3 - SDV4
Engineering Shear Strain - γ_{xy}	SDV5
Principal Strain - ϵ_1, ϵ_2	SDV6 - SDV7
Volumetric Strain - $\epsilon_1 + \epsilon_2$	SDV8
Axial Stress - σ_x, σ_y	SDV9 - SDV10
Shear Stress - τ_{xy}	SDV11
Strain Energy - ψ	SDV12
Elastic Strain energy - ψ_0	SDV13
Phase-Field - d	SDV14

Table 2.1: Solution Dependent Variables in Displacement Elements

Solution Dependent Variables (SDV) in Phase-Field Element	
Variable	2D (x,y)
Phase-Field - d	SDV15
History Field - H	SDV16

Table 2.2: Solution Dependent Variables in Phase-Field Elements

$(n+1)^{th}$ time step. Similarly, the damage value d_n obtained by the phase-field element at n^{th} time step is utilized by the displacement element to calculate displacement u_{n+1} & history function $\psi_{0,n+1}$ at the $(n+1)^{th}$ time step.
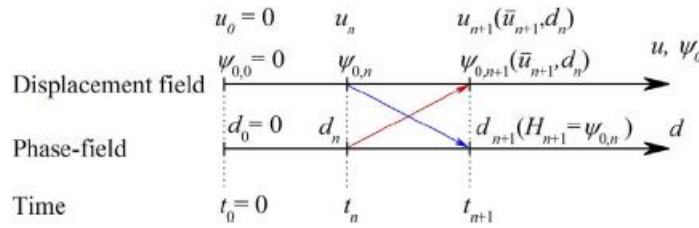

Figure 2.5: Iterative algorithm to solve the coupled displacement-phase-field solution
(Source: Molnar, [19])

15

Chapter 3

Phase-Field Fracture in Micro-Architectured Geometries

Looking at the high fracture strength, toughness and durability of natural materials like nacre, tooth and bones, many studies have been done to study their micro-structures [12 - 15]. It is seen that these materials have very intricate geometries with weak interfaces and are the reason behind the superior mechanical properties they possess. Inspired by these materials, Barthelat [12] tried to incorporate micro-structure in brittle materials with the intention of obtaining the same enhancement in mechanical properties as it can be seen in the above mentioned natural materials. Fig. 3.1 shows the interlocking jigsaw suture that Barthelat [12] introduced in ABS material. He gave an analytical traction-separation model for the shown jigsaw suture and compared the results with FEA and experimental results to verify the analytical model. It was seen that the traction-separation curves were strongly dependent on the friction coefficient (f) and the interlocking angle (θ_0). He also showed experimentally that the tabs break due to pull out at $\theta_0 = 20°$ and f = 0.35. In this chapter we are going to computationally simulate fracture in the tabs at $\theta_0 = 20°$ and f = 0.35 through the implementation of Phase-Field Fracture Model.
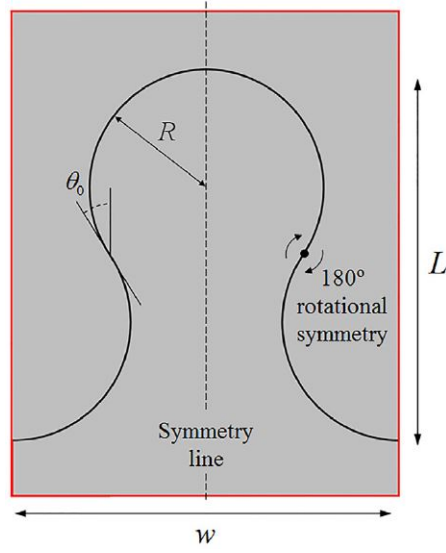
Figure 3.1: An interlocking jigsaw suture (Source: Barthelat, [12])

3.1 Interlocking Jigsaw Geometry

It can be seen that two tabs are connected to form a jigsaw like structure. The edges are rounded to avoid any stress concentration and the two tabs are connected in such a way that the blended edge makes an angle θ_0 with the vertical axis. Here, the interlocking angle θ_0 and friction coeffiecient f are the independent parameters and determine the tab length L, width w, pullout distance δ and strength as the tabs are in contact for a longer distance for larger interlocking angles θ_0 . The tab length and width can be represented as:

$$L = 2R(1 + sin\ \theta_0) \tag{3.1}$$

$$w = 4R\ cos\ \theta_0 \tag{3.2}$$

The value of θ_0 is greater than $0°$ and less than $60°$ [12]. If θ_0 is equal to $0°$ then there will be no interlocking and if it is greater than or equal to $60°$, the neck of the interlocking geometry intersects.
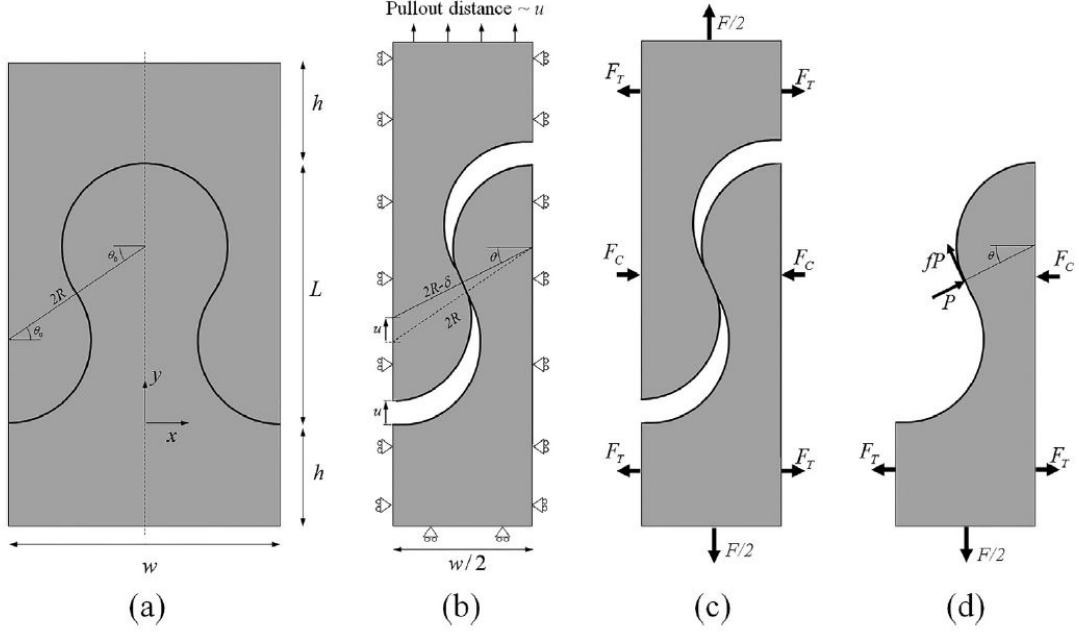
Figure 3.2: (a) Interlocking gigsaw geometry; (b) Symmetric form of the geometry in (a) with boundary conditions; (c) free body diagram of the symmetric geometry; (d) free body diagram of the lower tab. (Source: Barthelat, [12])

3.2 Analytical Model

In this analytical model by Barthelat [12], the pullout behavior of interlocking jigsaw geometry is studied. The material is considered to be isotropic and elastic. The interlocking geometry shown in Fig. 3.2 (a) has tab raidus R, interlocking angle θ_0, tab length L, tab width w, friction coefficient f and plate thickness t. Fig 3.2 (b) shows the same tab but in the symmetric form and with the necessary boundary conditions. The bottom edge is fixed in horizontal and vertical axes, the left and right edges are fixed in horizontal directions and a displacement u is applied at the top edge. δ is the interference between the two interlocking tabs when the top edge is displaced.

It can be assumed that the deformations near the contact is much larger in comparison to deformation in the bulk material. And based on this assumption we can give the kinematic equations for the pullout response that

18

connects initial and deformed configurations as,

$$(2R - \delta)\cos\ \theta = 2R\ sin\ \theta \tag{3.3}$$

$$u = 2R\ sin\ \theta_0 - (2R - \delta)\ sin\ \theta \tag{3.4}$$

Here, θ is the instantaneous angle generated by the line line joining the centres of the two tabs with the horizontal axis (Fig. 3.2 (b)) during the pullout. This θ varies from $+\theta$ to $-\theta$, such that, $+\theta$ represents the initial configuration and $-\theta$ represents the final state when the two tabs are completely pulled apart. It can also be seen that the distance between the two centers is $2R$ initially, but it reduces to $(2R - \delta)$ as the tabs are pulled apart. The interference δ produces a force that results in the force required for the pullout. But it also produces some horizontal force components on both sides of the model. However, these forces are balanced by tensile forces acting on the top and bottom part of the bulk as shown in Fig. 3.2 (c) ($F_c = 2F_t$). Further considering the normal force P and the frictional force fP as shown in Fig. 3.2 (d), the total pullout force can be given as,

$$F = 2P\ (sin\ \theta + f\ cos\ \theta) \tag{3.5}$$

Barthelat in his paper on bio-inspired interlocking sutures [12], gave the analytical formula for normalized pullout force (Eq. 3.6) and the normalized pullout distance (Eq. 3.7).

$$\frac{F}{wtE} = \frac{P}{RtE}(\frac{sin\ \theta + f\ cos\ \theta}{2\ cos\ \theta_0}) \tag{3.6}$$

$$\frac{u}{L} = \frac{sin\ \theta_0 - cos\ \theta_0\ tan\ \theta}{1 + sin\ \theta_0} \tag{3.7}$$

These quantities are used to generate the typical traction-separation curve for the analytical model as shown in Fig. 3.3. A sinusoidal curve is obtained for the frictionless case. This can be explained by the fact that only pullout force generated by the interference at the contact region is responsible for the traction. It can be seen that this pullout force starts acting downwards as the angle θ becomes zero or less. Due to this reason, the tensile force becomes compressive at $\theta = 0$ and we obtain a sinusoidal cure for the frictionless case. But when the friction at the contact surfaces is greater than 0, there is always a pullout force upwards that results in the nature of the traction curve to be tensile for a larger portion of the pullout distance. Once the friction

coefficient is greater than tan θ, the traction-separation curve is completely tensile and there is no compressive force throughout the separation of the tabs.
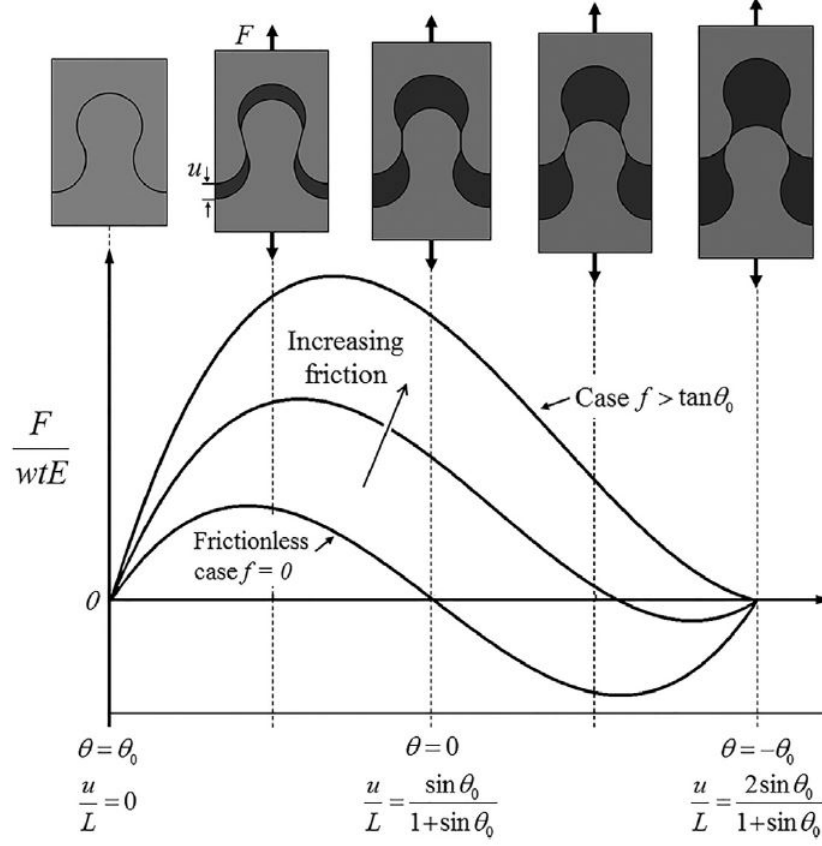

Figure 3.3: Traction separation curve obtained from the analytical model. (Source: Barthelat, [12])

3.3 Phase-Field Fracture modeling in interlocking jigsaw geometries using ABAQUS UEL

We implemented the Phase-Field fracture model using ABAQUS UEL as explained in Chapter 2. We performed Phase-Field FEA simulations on two

interlocking jigsaw specimen with different interlocking angles. The first specimen has 5° interlocking angle and the other one has 20°. The radius of tabs of the specimen were 1 mm for all the simulations and the plate thickness was 2 mm. Tab length and width can be easily calculated using Eq. (3.1) & (3.2). First, the FEA model was created using ABAQUS. We kept a gap of 0.5 micron between the interlocking tabs and applied surface-to-surface contact between the two interlocking edges. The meshing was done in such a way that the length scale parameter l_c was double (or even greater) than the the smallest mesh size [4]. The input file obtained from this model was modified according to the Phase-Field UEL using MATLAB.

3.3.1   5 degree interlocking angle

Four different simulations were run for the 5° interlocking angle specimen. The models were created exactly as mentioned above and the total displacement of 0.6 mm was given through 660 steps. The traction-separation response has been shown in Fig. 3.4 and Fig. 3.5 shows how the tabs completely get pulled out without any damage. It can be seen that the traction increases with an increase in the friction coefficient f and our FEA result matches with the analytical result. Now if we perform the same test on interlocking jigsaws with different interlocking angles, it can be clearly visible that the strength and energy absorption increase with the increase in interlocking angle θ_0. Thus, an increase in the interlocking angle and the friction coefficient results in an increase in the strength and energy absorption of the interlocking geometry. The higher interlocking angle θ_0 causes the two tabs to remain in contact for a longer time and thus results in the application of upward acting force for a longer duration. However, it is not the same if the friction coefficient increases. Friction coefficient has no effect on how long the two tabs remain in contact. But, the component of the frictional force acting towards the pull out direction increases with an increase in friction coefficient and thus results in an increased traction. Nonetheless, these parameters cannot be increased beyond a certain value as the generated high stresses can cause fracture in the tab before the completion of the pullout process. In section 3.3.2 we will study a scenario where there is a failure of tab due to certain interlocking angle and friction.
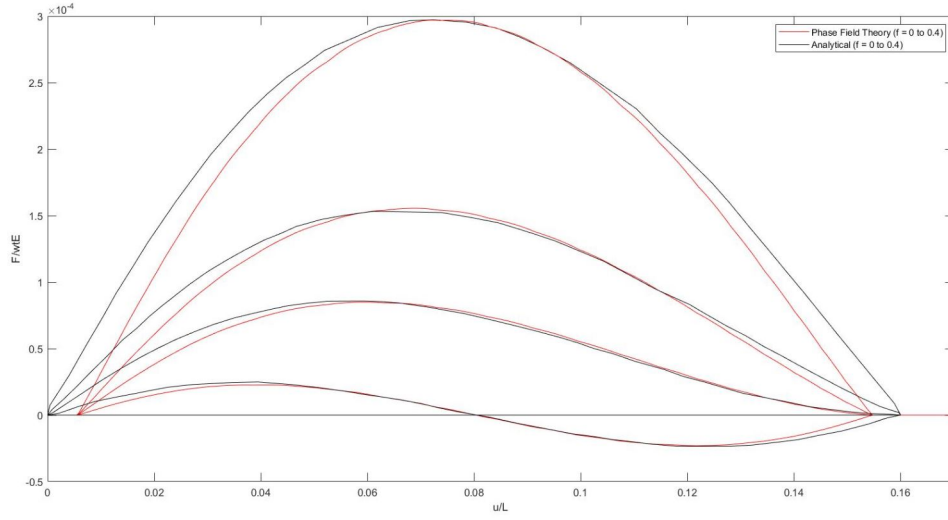
Figure 3.4: Traction-Separation curve for 5° interlocking angle obtained through Phase-field model vs. Analytical model
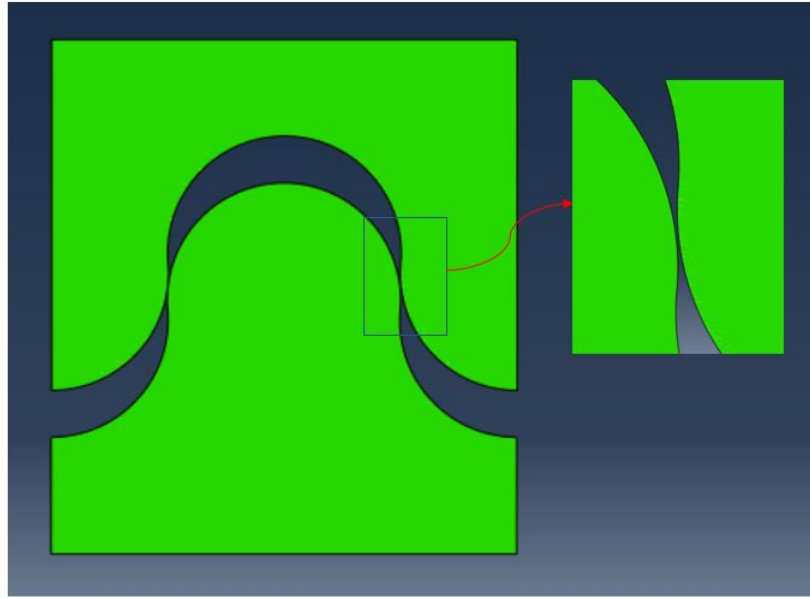

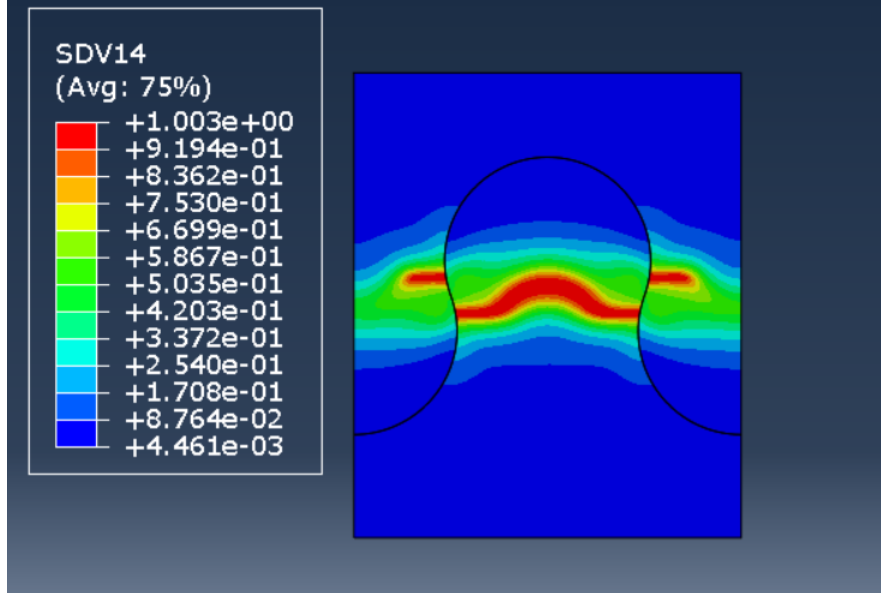Figure 3.5: Total pullout of the tabs with 5° interlocking angle

Figure 3.6: Fracture of tab with 20° interlocking angle

3.3.2   20 degree interlocking angle

The traction-separation curve for 5° interlocking angle proves that the Phase-Field model is working properly. The novelty of this work is the simulation of tab fracture using Phase-Field UEL. Barthelat [12] proved experimentally that the total pullout of tabs is not possible for all interlocking angles and friction coefficient values. He experimentally performed the tensile tests on interlocking geometries with 5°, 10°, 15° and 20° angles and with f = 0.35, E = 1.72 GPa and ν = 0.4. It was seen that the tabs with 5°, 10° and 15° angles separated completely without tab fracture at the end of pullout process, thus satisfying the analytical results. The fracture toughness and energy absorption increases with increase in θ_0 upto 15°. However, the tab for the interlocking jigsaw geometry fails at interlocking angle $\theta_0 = 20°$. In this study we implemented Phase-Field fracture model to simulate the fracture of the tab at 20° interlocking angle. We considered the following properties for this fracture modeling : E = 1.72 GPa, ν = 0.4, f = 0.35 and Energy release rate G_c = 0.1376 N/mm. It can be seen from Fig. 3.6 that the tab completely fractures in the middle where the damage (SDV14) value is equal to 1.
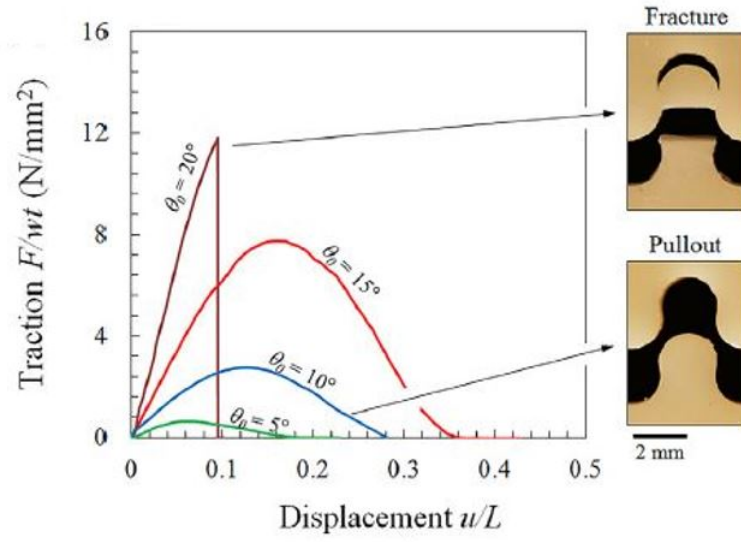
Figure 3.7: Traction-Separation plot of tab with 5°, 10°, 15° and 20° interlocking angle obtained by Barthelat [12] through experiments (Source: Barthelat [12])
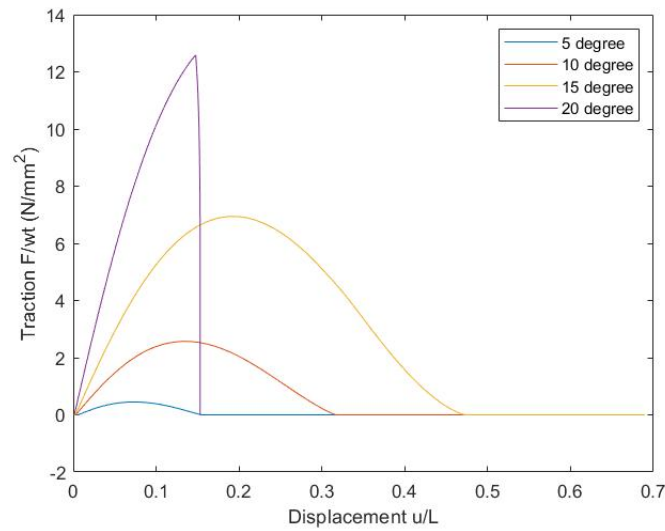

Figure 3.8: Traction-Separation plot of tab with 5°, 10°, 15° and 20° interlocking angle obtained through phase-field model

24

Traction-separation plot have also been provided in Fig. 3.7 and Fig. 3.8 for experimental and phase-field model results respectively. It is evident from the plot that the tab fails abruptly even before the force becomes compressive in nature for $20°$ interlocking angle. It is also evident that the phase-field fracture model simulates the experiment almost exactly.

Chapter 4

Conclusion

Staggered Phase-Field Fracture model was implemented through ABAQUS UEL to simulate fracture in micro-architectured materials. In this fracture model, crack is considered as a diffused/smeared damage rather than a sharp discontinuity. The staggered model incorporates two layers : displacement layer and phase-field layer. The layers utilize the required quantities from the previous time step to calculate the required solution in current time step. Apart from these layers, there is an additional UMAT layer that is applied for element visualization purposes.

Apart from fracture modeling, the other focus of this study was to understand the effect of interlocking angle and friction coefficient on the strength and energy absorption of the interlocking micro-architectured materials through computational simulations. It was found that with an increase in the interlocking angle and friction angle, the strength and energy absorption of the interlocking micro-architectured materials increased comprehensively. Nonetheless, there is a limit on the increase of these parameters. Based on previous experimental studies by Barthelat [12], it was seen that the tabs formed by these interlocking angles fails at $20°$ interlocking angle and 0.35 frictional coefficient. However, these results were obtained experimentally and not computationally. Thus, the primary focus of this research was to simulate this experiment computationally using Phase-Field Fracture model. By incorporating correct material properties, the fracture of tabs was simulated for $20°$ interlocking angle and 0.35 frictional coefficient.

Chapter 5

References

1. A.A. Griffith, The phenomena of rupture and flow in solids, Philos. Trans. R. Soc. Lond. A Math. Phys. Eng. Sci. 221 (582–593) (1921) 163–198.

2. G.R. Irwin, Fracture, Springer Berlin Heidelberg, Berlin, Heidelberg, 1958, pp.551–590.

3. B. Bourdin, G.A. Francfort, J.-J. Marigo, The Variational Approach to Fracture, Springer, Netherlands, 2008.

4. C. Miehe, F. Welschinger, M. Hofacker, Thermodynamically consistent phase-field models of fracture: variational principles and multi-field fe implementations, Int. J. Numer. Methods Eng. 83 (10) (2010) 1273–1311.

5. G.L. Peng, Y.H. Wang, A node split method for crack growth problem, Appl. Mech. Mater. 182–183 (2012) 1524–1528.

6. F. Zhou, J.F. Molinari, Dynamic crack propagation with cohesive elements: a methodology to address mesh dependency, Int. J. Numer. Methods Eng. 59 (1) (2004) 1–24.

7. D. Mumford, J. Shah, Optimal approximations by piecewise smooth functions and associated variational problems, Commun. Pure Appl. Math. 42 (5) (1989) 577–685.

8. G. Francfort, J.-J. Marigo, Revisiting brittle fracture as an energy minimization problem, J. Mech. Phys. Solids 46 (8) (1998) 1319–1342.

9. M. Buliga, Energy minimizing brittle crack propagation, J. Elast. 52 (3) (1998) 201.

10. B. Bourdin, G. Francfort, J.-J. Marigo, Numerical experiments in revisited brittle fracture, J. Mech. Phys. Solids 48 (4) (2000) 797–826.

11. G. Dal Maso, R. Toader, A model for the quasi-static growth of brittle fractures: existence and approximation results, Arch. Ration. Mech. Anal. 162 (2) (2002) 101–135.

12. Malik, I., Mirkhalaf, M., amp; Barthelat, F. (2017). Bio-inspired "jigsaw"-like interlocking sutures: Modeling, optimization, 3d printing and testing. Journal of the Mechanics and Physics of Solids, 102, 224-238. doi:10.1016/j.jmps.2017.03.003

13. Jackson, A. P., Vincent, J. F. V. Turner, R. M. The mechanical design of nacre. Proc. R. Soc. Lond. B 234, 415–440 (1988).

14. Koester, K.J. , Ager III, J.W. , Ritchie, R.O. , 2008. The true toughness of human cortical bone measured with realistically short cracks. Nat. Mater. 7 (8), 672–677 .

15. Bajaj, D. , et al. , 2010. Fracture processes and mechanisms of crack growth resistance in human enamel. Jom 62 (7), 76–82 .

16. Barthelat, F. , 2015. Architectured materials in engineering and biology: fabrication, structure, mechanics and performance. Int. Mater. Rev. 60 (8), 413–430 .

17. Mirkhalaf, M., Dastjerdi, A. K., amp; Barthelat, F. (2014). Overcoming the brittleness of glass through bio-inspiration and micro-architecture. Nature Communications, 5(1). doi:10.1038/ncomms4166

18. Valashani, S.M.M., Barthelat, F., 2015. A laser-engraved glass duplicating the structure, mechanics and performance of natural nacre. Bioinspirat. biomimet. 10 (2), 026005.

19. Molnár, G., amp; Gravouil, A. (2017). 2D and 3D ABAQUS implementation of a ROBUST staggered PHASE-FIELD solution for MODELING brittle fracture. Finite Elements in Analysis and Design, 130, 27-38. doi:10.1016/j.finel.2017.03.002